Extreme Mechanics Letters 34 (2020) 100598

Contents lists available at ScienceDirect

Extreme Mechanics Letters

journal homepage: www.elsevier.com/locate/eml

Spatial programming of defect distributions to enhance material failure characteristics

Chengyang Mo, Jordan R. Raney *

Department of Mechanical Engineering and Applied Mechanics, University of Pennsylvania, Philadelphia, PA, 19104, USA

A R T I C L E I N F O

Article history:
Received 5 August 2019
Received in revised form 30 October 2019
Accepted 31 October 2019
Available online 12 November 2019

Keywords:
Defects
Bioinspiration
Additive manufacturing
Architected materials

A B S T R A C T

Defects play a major role in determining the mechanical properties of materials. Examples of this span from dislocations, grain boundaries, and precipitates in metallurgy to voids and imperfect interfaces in natural composites. These can enable complex failure modes and balance competing mechanical properties. With the increasing adoption of additive manufacturing in both research and industry, there are unprecedented opportunities for controlling the internal composition and structure of a material system. However, the very nature of forming a material in increments produces a set of characteristic defects (e.g., void formation due to incomplete merger of new material), which results in local heterogeneity and anisotropy. Rather than seeking to prevent these characteristic defects, we utilize them to improve the damage resistance of printed structures by systematically controlling their distribution within a single material. Inspired by the well-known Bouligand structure found in tough natural materials, we use a helical build sequence in which each layer is added at a defined pitch angle relative to the previous layer. The resulting helical defect distribution can guide the crack tip during fracture and enhance damage resistance. Microstructural evidence from crack surface images and X-ray microtomography reveals intricate mixing of twisting and branching cracks during failure, and is explained via an analytical model. Since these improvements are obtained solely from the defect distribution within a single material, the findings of this work could improve the failure characteristics of a broad range of printed materials (metals, ceramics, polymers, and composites).

1. Introduction

Defects in engineering materials play a crucial role in determining their properties. In metals, defects such as grain boundaries and precipitates inhibit the propagation of dislocations, which can serve to increase strength (at the cost of decreasing ductility). In classical metallurgy, the nature and distribution of such defects can lead to order-of-magnitude changes in mechanical properties in otherwise identical materials, and mature process–structure–property relationships have been established. However, the importance of defects is much more general in materials engineering. For example, defects are also vital in natural materials, where voids [1] and imperfect interfaces [2] are responsible for producing excellent combinations of mechanical properties such as stiffness, strength, and toughness in materials that are also lightweight.

Numerous examples of this can be found in marine shell animals. For example, nacre consists of a classic brick and mortar arrangement of soft and stiff materials with imperfect interfaces [3]; conch shell has a hierarchical laminate structure [4]; and both the hammer-like Stomatopod dactyl club and the beetle exoskeleton include helical arrangements (the well-known "Bouligand" arrangement) of stiff chitin fibers within a matrix [5–7]. All of these comprise geometric arrangements of soft and stiff phases that enhance the toughness of the natural materials by impeding crack growth via combinations of multiple crack formation, crack deflection, and crack bridging.

The layer-by-layer design freedom afforded by additive manufacturing [8–10] and advances in multimaterial 3D printing [11, 12] allow, in principle, control over both the structure and composition within a printed material. The last several years have seen a number of studies that explore how some of these structural and compositional parameters affect failure in 3D printed materials. For example, a recent study used structural features inspired by polycrystalline metals (i.e., features resembling grain boundaries) to enhance failure properties in 3D printed structures [13]. The influence of structural hierarchy on failure has been explored [14]. 3D printing has also been used to study the mechanics of bioinspired architectures. For example, artificial marine stickleback armor [15] and Turritella shell [16] have been 3D printed to better understand the influence of geometry on the robustness of these natural materials. With multimaterial 3D printing it is possible to enhance the toughness of materials

---

* Corresponding author.
E-mail address: raney@seas.upenn.edu (J.R. Raney).

https://doi.org/10.1016/j.eml.2019.100598

by arranging soft and stiff phases in architectures that mimic natural motifs, such as that of conch shell [17], nacre [18], and Stomatopod dactyl club [19]. Bioinspired composites such as glass fiber-reinforced polymers [20], alumina-reinforced polymers [21], and epoxy-carbon fiber [22] have also been developed for direct write 3D printing processes [8,12].

Regardless of the specific additive manufacturing approach, however, the very nature of adding (or selectively solidifying) material in increments inevitably produces *systematic* defects that are intrinsic to a given additive process and the chosen build sequence. For example, in extrusion-based additive manufacturing processes illustrated in Fig. 1a, such as direct ink writing (DIW) [8] and fused deposition modeling (FDM) [9], filaments of material are extruded by nozzles that translate relative to a substrate to form a pattern. Geometric defects (e.g., voids) can arise due to incomplete merger of extruded filaments, and material anisotropy is common due to imperfect bonding between adjacent filaments (particularly in FDM). In additive manufacturing processes that require *in situ* heating, such as FDM [23,24] and selective laser sintering (SLS) [25,26], non-uniform heating is also a mechanism of defect formation, resulting in anisotropic residual stresses and material heterogeneity [24,25]. Geometric defects can often be observed via non-destructive methods such as X-ray microtomography (μCT) or via imaging of fracture surfaces post failure (inset, Fig. 1a). Because both geometric defects and material heterogeneities are systematic (and determined by the build sequence used in the additive process), they produce characteristic material anisotropy. One well-known example of this is the reduction in strength that is observed transverse to the infill/raster direction in additive processes [23,25].

As we show here, these characteristic defects can be arranged to enhance the damage resistance of printed structures. The idea of programming the spatial distribution of defects to improve mechanical properties has been demonstrated in brittle glass via laser etching of 2D patterns within the material [27]. Here, we spatially control the distribution of defects in 3D via the build sequence used during additive manufacturing. We make use of the well-known Bouligand structure (Fig. 1b), which can enhance toughness via formation of multiple cracks and the mixing of fracture modes at the crack fronts [28]. During failure, the defects can act as stress concentrators, guiding the failure process in ways that activate the same Bouligand toughening mechanisms that are observed in other contexts. The geometric defects can also alter the stress field around the crack tip and enhance toughness via extrinsic mechanisms such as crack shielding [29]. As discussed previously, there are numerous examples of *multimaterial* architectures in the literature [19,20,30], often inspired by natural composites, that use material mismatches to activate toughening mechanisms. However, the complexity of the processes and the lack of control over the interfacial properties (intrinsic to the materials) often limit the practical utility of these approaches. Here, comparable toughening enhancements are accomplished solely via the programmable arrangement of the defects, which produce locally-anisotropic mechanical properties of the same sort sought in multimaterial architectures but in single-material systems that are simple to fabricate and require no post-processing (e.g., laser etching). Since it is the defects rather than specific material pairings that produce the desired properties the findings of this work are relevant to a broad swathe of additive manufacturing processes (FDM, DIW, SLS, etc.) and materials (polymers, metals, ceramics, and composites).

2. Experimental results

As a proof of concept, we first printed conventional single-edge notched bend (SENB) samples, which include a notch to predictably initiate fracture in the center of the sample during bending (see Fig. 1c). To illustrate the large effect that the defect distribution has on the failure properties, we used a helical (Bouligand) print pattern in front of the notch tip, with each infill layer printed with a raster pattern oriented by a constant pitch angle γ relative to the previous layer. The orientation of each infill layer can be described by infill angle ϕ, the angle between the filaments and the Z-axis. The initial infill angle of the first layer in front of the crack tip is defined as ϕ_0. The notch induces the onset of fracture directly into the Bouligand region. After fabrication, the samples were loaded in three-point bending until failure (Fig. 1c–d). We used two different additive processes to show the relevance of the defect distribution in two very different materials systems: quasi-brittle thermoplastic poly-lactic acid (PLA), which was printed using a commercial fused deposition modeling printer, and the elastomer polydimethylsiloxane (PDMS), which was printed using direct write 3D printing. As in Fig. 1d, the propagation of the crack preferentially follows the helicoidal defect distribution (without requiring the use of a second material to produce internal material interfaces, as in previous studies). Despite the extremely different properties in these two materials (a relatively brittle PLA and a soft, ductile silicone elastomer) we observe qualitatively similar failure surfaces due to the controlled distribution of defects (Fig. 1d).

To understand why the helicoidal raster pattern leads to this behavior, we first characterized the effect of the raster angle on the in-plane elastic properties of the printed structures. For this analysis, we chose to focus on the PLA system, since the very high failure strain of the PDMS makes these soft materials less amenable to studying bending failure. We first printed tensile bars from PLA using different constant raster angles (with the angles defined relative to the direction in which loading was applied.) and performed quasistatic tensile tests on these. The raster angle has a large effect on the mechanical properties, as expected, due to the high degree of anisotropy associated with the interfilament defects. For example, "longitudinal" samples (in which the raster angle is parallel with the direction of mechanical loading) and "transverse" samples (in which the raster angle is perpendicular to the direction of loading) differ in stiffness and strength by 22.5% and 53.8%, respectively (see details in Table S1 and Fig. S1).

Next, we printed SENB samples from PLA with a Bouligand structure in front of the notch. We varied the pitch angle and tested these to failure. As controls, we first tested SENB samples of only a single raster angle ($\gamma = 0°$ no helicoidal or Bouligand structure). These included two types of samples: First, $\phi_0 = 0°$, with all printed filaments (and therefore the interfilament defects) aligned with the notch; second, $\phi_0 = 90°$, with all printed filaments (and interfilament defects) oriented perpendicular to the notch. The load–displacement data for both the Bouligand samples and the two types of control samples are shown in Fig. 1e. The corresponding fracture properties are plotted in Fig. 1f and g. The fracture toughness, which directly corresponds to the peak force the structure can withstand and the geometry of the structure [31], quantifies how difficult it is for a crack to initiate in a structure, and the energy dissipation (or toughness) corresponds to the area under the load–displacement curve, indicating the total amount of energy required to fracture the sample. Looking at the control samples, it is evident that the first type ($\phi_0 = 0°$, distributing the defects parallel with the notch) fracture easily and dissipate very little energy during failure. Once initiated, the crack propagates straight along a defect through the entirety of the structure. In the second case ($\phi_0 = 90°$, distributing the defects perpendicular to the notch) the samples show very high fracture toughness (i.e., it is difficult for the cracks to initially form and propagate). However, these also have low energy dissipation,

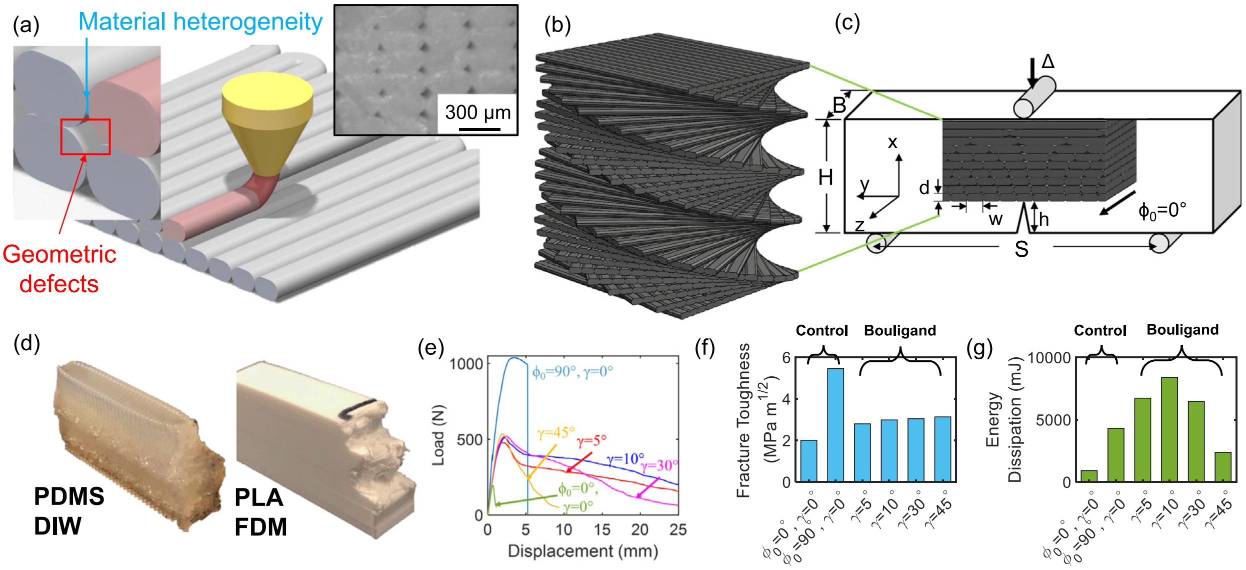

Fig. 1. (a) Illustration of an extrusion-based additive manufacturing process with its characteristic systematic distribution of defects; inset is a microscope image showing the defect distribution between filaments within a plane perpendicular to the filaments; (b) Schematic of Bouligand structure; (c) Schematic of the single-edge notched bend (SENB) experimental tests, including the geometric parameters of the samples and the definitions of coordinates; (d) Photographs of samples after testing, showing similar fracture surfaces from two different materials (PLA and PDMS) printed with two different additive processes (FDM and DIW, respectively); (e) Load–displacement behavior of PLA samples as measured during SENB tests; (f) Fracture toughness of the PLA samples; (g) Energy dissipation of the PLA samples.

as the samples fail immediately after reaching the peak load. The large discrepancy in fracture toughness between the two control samples means there is a preferred direction (being $\phi = 0°$) for crack propagation within each region of the structure with constant raster angle. For the Bouligand structures, pitch angles of $\gamma = 5°$, $10°$, $30°$, and $45°$ were used, with the infill angle of the first layer aligned with the crack front ($\phi_0 = 0°$). (A larger pitch angle will result in more periods within a given number of layers. Images of samples with different pitch angle are shown in Fig. S3 where the periodicity can be clearly observed, particularly for lower pitch angles.) In contrast with the control samples, The fracture toughness of the Bouligand samples do not show significant variations (regardless of pitch angle γ). However the energy dissipation of all but one type of Bouligand structure exceeds that of the control samples. During the test, these structures showed extreme resilience and did not catastrophically fail even as the deflection reached up to 25 mm (equivalent to a bending angle of 83.6°). The samples with a pitch angle of 10° showed the maximum amount of energy dissipation (2.25 times higher than the unidirectional control samples with $\phi_0 = 90°$ and 10 times higher than the unidirectional control samples with $\phi_0 = 0°$).

The properties of the defects between the filaments can significantly affect the fracture properties. To confirm this, we altered the properties of the defects between filaments, alleviating material heterogeneity by post-processing (thermal annealing) and changing the size of the geometric defects (associated with the imperfect merger of filaments) by adjusting print parameters (specifically, filament spacing). As expected, changing the defects (e.g., their average size) does indeed change the failure characteristics (details in Fig. S4). This suggests that there is an optimal defect size for obtaining the maximal toughness: If defects are too small they do not generate sufficient anisotropy to control the fracture mode (twisting vs. branching); if defects are too large then adjacent layers of filaments do not transfer sufficient stress. This also shows that the arrangement of the characteristic defects is responsible for the changes in failure properties.

3. Analysis

To better understand the toughening mechanism in the Bouligand portions of our structures, here we examine the fracture behavior analytically, with the goal of qualitatively capturing the most essential features of the failure surface. While the fracture of Bouligand structures comprising multiple materials has been previously studied [20], here we show that it is not necessary to have a complex multimaterial composite to achieve toughening: a Bouligand-like 3D distribution of defects in a single-material system produces the same result. It is the *local anisotropy* that is essential for producing the toughening (which can be achieved either by interfaces between dissimilar materials or by defects), not interfaces between multiple materials. In order to understand the key characteristics of the crack behavior, we assume a simplified, flat crack front, twisted under global Mode-I loading and propagating through a linear, elastically-isotropic material, similar assumptions as in previous work [28]. The assumption that the material is elastically isotropic has minimal effect on our results, since, as we have shown in the SI, the anisotropy of the elastic properties of the printed layers is rather small. We also assume a helical crack pattern of the form $Y = -Z \tan \frac{d\phi}{dX} X$ (using the coordinates described in Fig. 2a), where $\frac{d\phi}{dX}$ defines the pitch of the helical surface. With the crack propagating in the X direction, the twisting angle α describes the angle between the XZ plane and the point on the crack front while the angle ϕ describes the twisting of the crack front with respect to the X direction. These two angles can describe the ratio of the local energy release rate (G_0) and the global Mode-I energy release rate (G_I):

$$\frac{G_0}{G_I} = g(\phi, \alpha) = \left(\frac{k_I'}{K_I}\right)^2 + \left(\frac{k_{II}'}{K_I}\right)^2 + \frac{1}{1-\nu}\left(\frac{k_{III}'}{K_I}\right)^2 \tag{1}$$

where K_I is the applied Mode-I stress intensity factor and ν is the Poisson's ratio. The local stress intensity factor k_I', k_{II}', and k_{III}' are computed with twisting angles (ϕ and α):

$$\begin{aligned} \frac{k_I'}{K_I} &= \cos\frac{\alpha}{2}\left[\cos^2\frac{\alpha}{2}\cos^2\phi + 2\nu\sin^2\phi\right] \\ \frac{k_{II}'}{K_I} &= \sin\frac{\alpha}{2}\cos^2\frac{\alpha}{2}\cos\phi \\ \frac{k_{III}'}{K_I} &= \cos\frac{\alpha}{2}\sin\phi\cos\phi\left[\cos^2\frac{\alpha}{2} - 2\nu\right] \end{aligned} \tag{2}$$

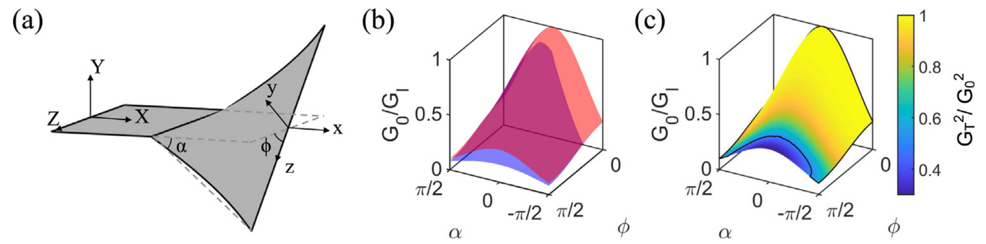

Fig. 2. (a) Schematic of the twisting angle ahead of the crack tip; (b) surface plot ratio of G_0/G_I vs. ϕ and α (the magenta surface corresponds to the analysis in this work; the blue surface is plotted from the results of Ref. [20]) and (c) contour plot of $(G_T/G_0)^2$ on the surface of G_0/G_I. (For interpretation of the references to color in this figure legend, the reader is referred to the web version of this article.)

In our structures, each infill layer of unidirectional filaments has two possible failure modes. The first mode consists of fracture parallel with the filaments (typically along the defects that exist between the filaments). In Bouligand structures with a different filament orientation for each layer, this leads to a twisting crack as the crack tip propagates from layer to layer. We therefore refer to this type of failure as a *twisting* mode (energy release rate corresponding to this mode is G_T). The other distinct failure mode is fracture perpendicular to the filaments. In a Bouligand architecture this can lead to a sharp translation or splitting of the crack tip. We therefore refer to this type of behavior as a *branching* mode (energy release rate corresponding to this mode is G_B). The branching mode is much tougher and stronger, as measured experimentally (Fig. 1f and g). As a crack propagates it may move from one failure mode to the other based on the local conditions. For example, a crack propagating in the twisting mode may occasionally branch, as observed previously in composites [28]. We assume a mixed fracture criterion with a square form that includes both fracture modes:

$$\left(\frac{G_T}{G_{T,c}}\right)^2+\left(\frac{G_B}{G_{B,c}}\right)^2=1 \tag{3}$$

Note from Eq. (1) that $G_T/G_I = g(\phi,\alpha)$ is a function of the twisting angle ϕ and α. The local coordinate for the branching mode involves a rotation of $\pi/2$ about the local X axis. Hence the local effective energy release rate for branch mode can be described by the same α of the twisting mode and $\phi' = \phi + \pi/2$ with $G_B/G_I = g(\phi',\alpha)$. Now by multiplying Eq. (3) by $(G_{T,c}/G_I)^2$ and plugging in these two expressions, we obtain the local fracture criterion:

$$\frac{G_0}{G_I}=\sqrt{g^2(\phi,\alpha)+\left(\frac{G_{T,c}}{G_{B,c}}g(\phi+\pi/2,\alpha)\right)^2} \tag{4}$$

To compute the ratio between the two critical energy release rates $G_{T,c}/G_{B,c}$, we can find the critical energy release rate for the two cases $G_{T,c}$ and $G_{B,c}$ where $G_c = \frac{K_{IC}^2}{E}$ by assuming a linear elastic material. The stiffnesses for the twisting mode and the branching mode are simply those of the transverse and longitudinal samples, respectively. Unlike the case presented previously [28], which involved a soft matrix, the strength ratio between our two fracture modes might prefer filament breakage as the crack tip twists. The local fracture criterion in Eq. (4) is plotted in Fig. 2b. The prior analytical result [28] is also plotted here as the blue surface. Note our criterion is generally larger than the previous work (indicating it requires less external loading for the crack to propagate) since we allow an additional failure mechanism not considered previously. Moreover, we can see that the ratio $G_0/G_I \approx 1$ at the center of the crack when $\phi = 0°$, indicating that the crack would prefer to fail completely along the filaments initially ($\phi = 0°$). As the crack grows the contribution from the longitudinal fracture increases the load required to propagate the crack (effectively decreasing G_0/G_I). Additional information can be extracted from Fig. 2c as the contribution from the twisting mode $(G_T/G_0)^2$ is plotted as a surface contour. Note, when the ratio is 0.5, both failure modes contribute equally. In this plot, the black line partitions the twisting angle into two spaces where each failure mode is preferred. In our case, when the filament becomes perpendicular to the crack front ($\phi = 90°$) our structure would prefer to break the filament (fail in the branching mode) rather than propagate in the twisting mode.

4. Microstructural evolution during failure

In addition to the above experiments and analysis, we characterized the fracture surfaces after failure, and at different stages during failure, to determine whether the failure characteristics match the model. First, Fig. 3 shows schematics of infill angles at the fracture surfaces for various pitch angles and their corresponding periodicities. Fig. 3 also shows optical images of the fracture surfaces after complete failure. For pitch angles of 5° and 10° (Fig. 3a and b), a complex 3D fracture surface is observed, with crack propagation both in and out of plane. The dashed lines in Fig. 3a and b indicate the distance over which the given pitch angle leads to a complete revolution of the helical Bouligand structure. Interestingly, the fracture surface indicates that the crack clearly twists within each indicated period. The crack surfaces also reveal the expected twisting mode as $\phi \to 0°$ and the branching mode as $\phi \to 90°$ as predicted in Fig. 3a and b in accordance with our previous analysis. The crack surfaces for samples with pitch angles of 30° and 45° (Fig. 3c and d, respectively) show less out-of-plane variation, with more uniform filament breakage and pullout.

More details about the crack propagation and toughening mechanisms can be obtained by measuring the internal crack growth at different stages of failure (see Fig. 4). To do this, six identical SENB samples were fabricated with the same pitch angle ($\gamma = 10°$). These were tested under the same loading conditions, but with the loading halted at various stages of deformation (see the numbered points in Fig. 4a, indicating where the testing was stopped for each of the six samples). The initial load–displacement curves for all of the samples are very similar, with the average load shown in black, and the standard deviation of the load plotted in gray around it (Fig. 4a). After loading, each sample was subsequently scanned in μCT to identify how the crack and the morphology of the material surrounding it change as a function of displacement. From these data we first extracted the crack length (in the X direction) for each sample. Using this information together with the load–displacement data for each sample, we calculate the strain energy release rate J (Fig. 4b). The energy release rate shows a clear bilinear behavior, indicating that an increased driving force is required as the crack propagates. This implies that extrinsic toughening mechanisms are present in our structure [32] similar to mechanisms in natural materials [3,4] and other bioinspired composites [33]. To explain the transition in energy release rate and the transition in crack

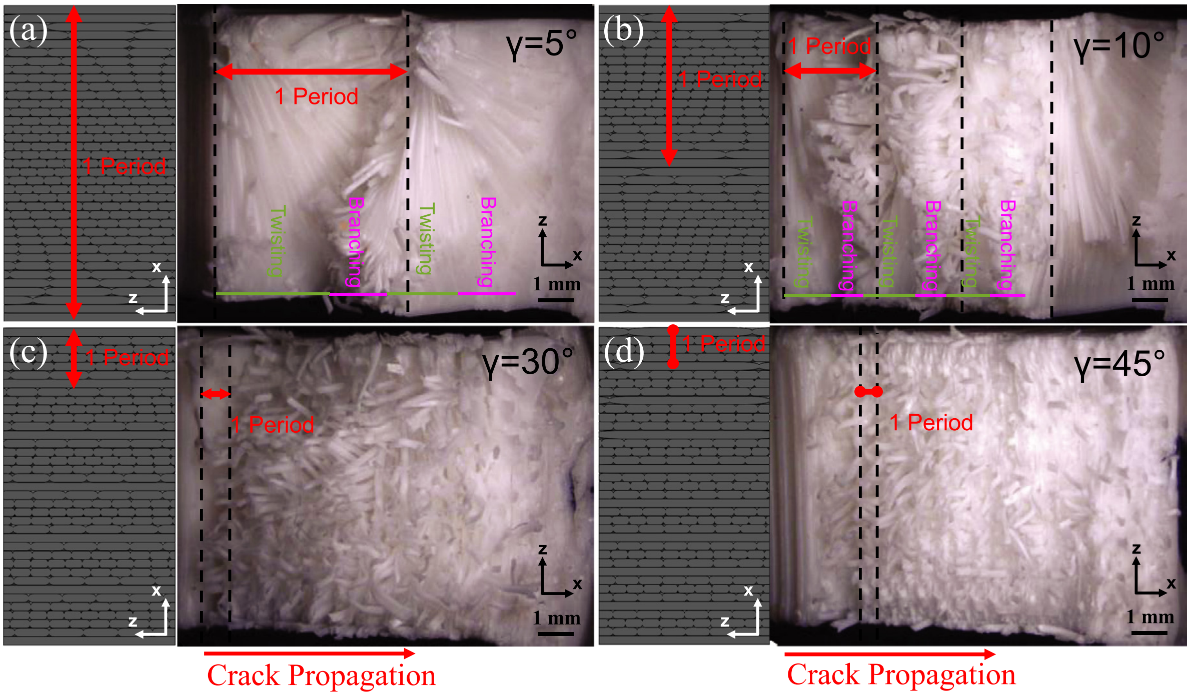

Fig. 3. Schematic of filament orientations and optical images of the fracture surface for samples of all pitch angles: (a) 5°, (b) 10°, (c) 30°, and (d) 45°. The initial crack front is located at the left of each image. Enlarged versions of these images are shown in Fig. S5 without annotations.

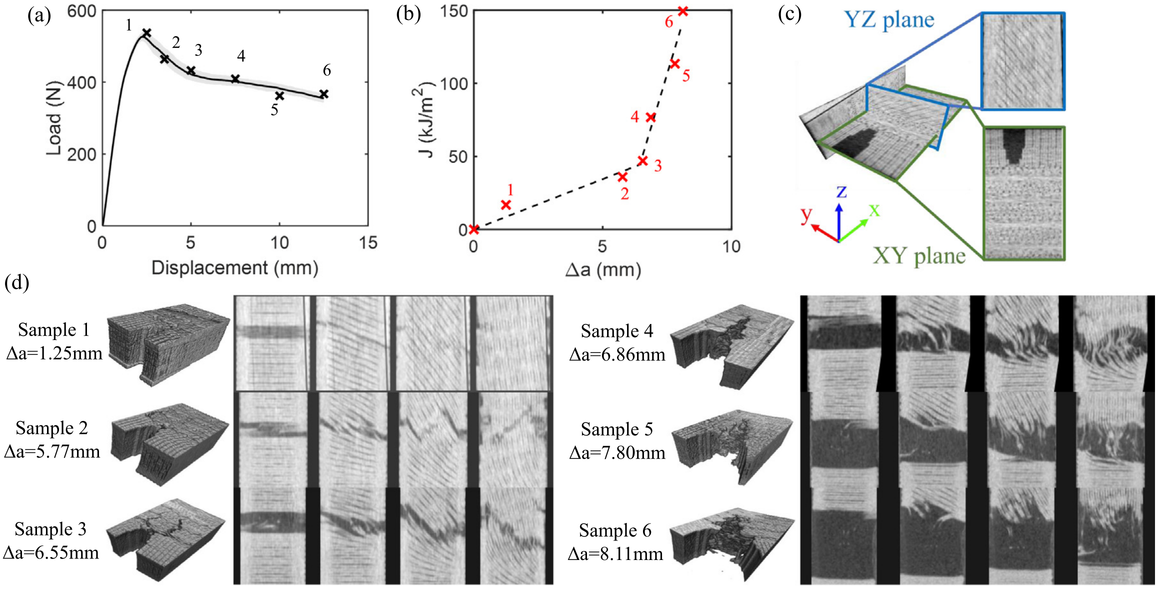

Fig. 4. μCT data for six samples (with pitch angle $\gamma = 10^\circ$). (a) For each of the six samples the fracture testing was halted at one of the six indicated positions; (b) the energy release rate; (c) illustration of μCT result datum planes; (d) 3D reconstruction of the μCT data at the crack front region, and YZ slices ahead of the original crack front.

behavior at the critical point where the slope sharply changes, we rely on information obtained via μCT, specifically regarding the YZ plane (as shown in Fig. 4c).

In Fig. 4d we show the crack region in the YZ plane which lies directly in front of the initial notch. Sample 1 (loaded to the peak load in Fig. 4a, but not beyond it) shows minimal damage with a very short crack. The crack grows by a factor of three as the load–displacement curve moves from Point 1 to Point 2 (Fig. 4a). In the YZ plane, the crack is initially observed to follow the filament direction (similar to a twisting crack). However, in the third cross section of Sample 2 ($\phi \approx 45^\circ$) both the twisting mode and the branching mode are observed (the center filaments follow the branching mode while the side filaments follow the twisting mode). The analytical model predicts that as ϕ increases there is an increasing contribution from the branching mode, and that such an effect is strongest at the center of the sample ($\alpha = 0^\circ$), as shown in Fig. 2c. This effect is even more clear in the fourth cross section ($\phi \approx 85^\circ$) as the center crack associated with the branching mode is longer than that seen in the third cross-section, providing a larger region that is favored to propagate cracks in the branching mode. The crack path for Sample 3 is slightly different than for Sample 2, as a twisting mode seems to propagate on the left hand side and a branching mode on the right hand side. This could be the result of the propagation of two separate cracks, which can be seen in the 3D reconstruction of the μCT for Sample 3. Nevertheless, it still supports our previous observation of an increasing contribution from crack branching as the crack propagates. The crack surfaces for the first three samples show that the structure is toughened by both twisting and branching cracks, accordingly producing the complex fracture surfaces observed in Figs. 3 and 4.

Referring to Fig. 4b, the crack length for Sample 3 is very close to the critical length at which the strain energy release rate J transitions to the higher slope of the second linear region. For the higher displacements of Samples 4–6, all of which correspond to the second (high-slope) region of the strain energy release rate in Fig. 4b, the load–displacement behavior shows minimal load drop as the sample deforms (Fig. 4a). From the μCT results it is clear that this regime is associated with very slow crack growth. The layers ahead of the initial crack tip realign in the direction perpendicular to the crack front, which is especially clear in the cross-sectional images for Sample 4. This effect could be the result of multiple twisting cracks formed within a single layer. As the loading continues, the filaments have the freedom to align perpendicular to the original crack front, increasing the driving force required for the crack to propagate further. This also explains the large residual loads (after passing the peak load) in the load–displacement curves of these samples with pitch angle $\gamma = 10^\circ$. For a smaller pitch angle such as $\gamma = 5^\circ$, more layers fail in the twisting mode as the crack propagates. This means there should be less residual load after passing through the peak load. This is precisely what is observed in Fig. 1e. For a pitch angle of $\gamma = 30^\circ$ the stiffness difference between two subsequent layers is much larger, and therefore failure can also occur between each layer.

5. Toward optimized, heterogeneous defect distributions

Based on the fracture properties presented in Fig. 1, the Bouligand defect distribution achieves higher energy dissipation (toughness) but does so at the cost of decreased strength and fracture toughness, reflecting the classic materials tradeoff [32]. Natural materials, however, are not uniform: they utilize highly-optimized composite architectures that are heterogeneously distributed to maximize mechanical and physical properties for a given set of loading conditions. Likewise, additive manufacturing can be used to heterogeneously distribute different motifs to maximize mechanical performance. Bouligand structure (such as in the Stomatopod club) plays a vital role in increasing the energy required to continue the propagation of a crack. However, the structure is not ideal for preventing the formation of a crack tip in the first place. For this reason, natural materials combine Bouligand structures with other motifs with higher local strength (but more brittle failure) such as a hard shell, which act as the first layer of defense [5]. Making use of the layer-by-layer freedom of additive methods, we mimic this strategy observed in natural composites by printing heterogeneous structures as illustrated in Fig. 5a. A unidirectional region (UR) is placed perpendicular to the notch, where its high stiffness and strength (yet brittle failure profile) serves to delay the onset of the crack, producing maximum strength during crack initiation. Subsequently, once the crack forms and propagates through this first region, it reaches the periodic region (PR) where the defects are arranged in Bouligand form (in this case using a pitch angle of 10°), which increases the energy required for the crack to continue propagating. Together, this heterogeneous structure achieves fracture properties that avoid the pitfalls of either a pure bouligand (PR) structure, with its high energy dissipation but low fracture toughness, or a pure unidirectional print (UR), with its high strength and fracture toughness but low energy dissipation (Fig. 5b). This simple example illustrates how additive manufacturing could be married to modern design and optimization techniques to produce optimal heterogeneous defect distributions for maximal combinations of target properties (such as high strength and toughness).

Just as defects play an essential role in determining the mechanical properties of metals, ceramics, and composites fabricated via traditional manufacturing processes, the same is true for materials produced via additive processes. Additive manufacturing unavoidably introduces characteristic, systematic defects based on the build sequence. By arranging these defects in a geometric motif inspired by natural materials, we achieved toughening mechanisms (intricate crack path and mixed loading at crack tips) comparable to those observed in natural materials and in bioinspired composites. Moreover, by spatially varying the defect distribution (as observed in natural materials) one can in principle optimize for maximal combinations of strength and toughness. Unlike previous research, which focused on multimaterial 3D printing, which is highly materials specific (for example, the ratio of stiffness between the two materials, the interfacial adhesion, etc.), we have shown that the defect distribution alone can be controlled to enhance the failure characteristics even in single-material systems. These results are therefore relevant to a wide variety of materials systems and additive approaches.

Materials and methods

FDM printing

The structures are printed with a commercial FDM printer (Makergear M2) with PLA (Hatchbox 1.75 mm filaments) using a 0.25 mm diameter nozzle heated to 190 ° C on a heated bead (60 ° C). Each printed filament has a width (w) of approximately 0.3 mm and a layer height (d) of 0.15 mm.

DIW printing

PDMS, consisting of 85% SE1700 and 15% Sylgard 184 (Dow Corning), was printed via DIW following a previously-developed procedure (see, e.g., Ref. [34]). To enhance the mechanical anisotropy of the structure, a small region (1 mm wide) within the center of each layer is printed using PDMS with a lower concentration of curing agent (ratio of 15:1 resin to curing agent instead of 10:1). Printed structures are cured at 100 °C for 3 h.

Mechanical testing

Mechanical testing is conducted using an Instron Model 5564 operating in displacement control for both tensile and bending tests. Tensile tests are conducted with a strain rate of 0.0015 s^{-1}. Bending tests are conducted with a displacement rate of 2 mm/min.

X-ray microtomography

μCT is conducted using a Scanco VivaCT 80 at a spatial resolution of 78 μm. All six samples were placed inside an 80 mm diameter tube. Scan data are saved as tiff images and subsequently analyzed using MATLAB.

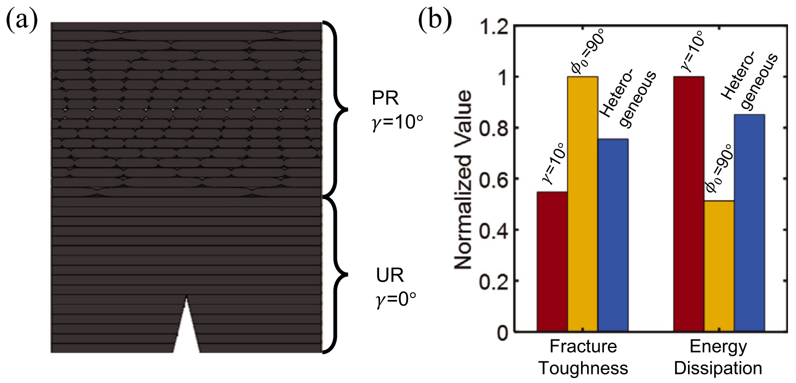

Fig. 5. (a) Illustration of a bioinspired, heterogeneous sample including a high-strength (but more brittle) unidirectional region directly in front of the notch (designed to inhibit crack initiation), and a Bouligand region beyond it (designed to increase the energy cost for a crack to continue propagating once initiated); (b) Normalized fracture properties for the Bouligand structure with pitch angle $\gamma = 10°$ (with the highest energy dissipation), the unidirectional structure with $\phi_0 = 90°$ (with the highest fracture toughness), and a heterogeneous structure that combines both.

Fracture property calculation

Fracture toughness of the SENB sample is calculated from the geometry and peak load P following ASTM-E399-17: $K_I = PS/(BH^{3/2})f(a/W)$, where f is a non-dimensional geometric factor [31]. The energy release rate J is calculated stepwise using the measured crack length a, the area under the load displacement curve A_{pl}, and ligament $b \equiv H - a$: $J_{pl(i)} = [J_{pl(i-1)} + (1.9/b_{(i-1)})(A_{pl(i)} - A_{pl(i-1)})/B][1 - (a_{(i)} - a_{(i-1)})/b_{i-1}]$ [33].

Data availability

Data, documentation, and code used in analysis is available upon request.

Declaration of competing interest

The authors declare that they have no known competing financial interests or personal relationships that could have appeared to influence the work reported in this paper.

Acknowledgments

This research was partially supported by the National Science Foundation (NSF) through the University of Pennsylvania Materials Research Science and Engineering Center (MRSEC) (DMR-1720530) and by a 3M Non-Tenured Faculty Award. The authors thank Dr. Karen Winey and Lu Yan for use of the materials test system. The authors also thank Dr. Sherry Liu, Wei-ju Tseng and Carlos Osuna for assistance with μCT, and the funding source for operating the μCT equipment: Penn Center for Musculoskeletal Disorders (NIH/NIAMS P30 AR069619).

Appendix A. Supplementary data

Supplementary material related to this article can be found online at https://doi.org/10.1016/j.eml.2019.100598.

References

[1] M.K. Habibi, Y. Lu, Crack propagation in bamboo's hierarchical cellular structure, Sci. Rep. 4 (2014).

[2] F. Barthelat, A.K. Dastjerdi, R. Rabiei, An improved failure criterion for biological and engineered staggered composites, J. R. Soc. Interface 10 (79) 20120849.

[3] F. Barthelat, H. Tang, P.D. Zavattieri, C.M. Li, H.D. Espinosa, On the mechanics of mother-of-pearl: A key feature in the material hierarchical structure, J. Mech. Phys. Solids 55 (2) (2007) 306–337.

[4] S. Kamat, X. Su, R. Ballarini, A.H. Heuer, Structural basis for the fracture toughness of the shell of the conch Strombus gigas, Nature 405 (6790) (2000) 1036–1040.

[5] J.C. Weaver, G.W. Milliron, A. Miserez, K. Evans-lutterodt, S. Herrera, I. Gallana, W.J. Mershon, B. Swanson, P. Zavattieri, E. Dimasi, D. Kisailus, The stomatopod dactyl club: A formidable damage-tolerant biological hammer, Science 336 (June) (2012) 1275–1280.

[6] L.K. Grunenfelder, E.E. De Obaldia, Q. Wang, D. Li, B. Weden, C. Salinas, R. Wuhrer, P. Zavattieri, D. Kisailus, Stress and damage mitigation from oriented nanostructures within the radular teeth of cryptochiton stelleri, Adv. Funct. Mater. 24 (39) (2014) 6093–6104.

[7] J. Sun, B. Bhushan, Structure and mechanical properties of beetle wings: A review, RSC Adv. 2 (33) (2012) 12606–12623.

[8] J.A. Lewis, Direct ink writing of 3D functional materials, Adv. Funct. Mater. 16 (2006) 2193–2204.

[9] S.S. Crump, Apparatus and method for creating three-dimensional objects, U.S. Patent No. 5121329 A, 1992.

[10] C.W. Hull, Apparatus for production of three-dimensional objects by stereolithography, U.S. patent No. 4575330A, 1986.

[11] R. Wicker, F. Medina, C. Elkins, Methods for multi-material stereolithography, U.S. patent No. 7959847B2, 1986.

[12] J.R. Raney, J.A. Lewis, Printing mesoscale architectures, MRS Bull. 40 (11) (2015) 943–950.

[13] M.S. Pham, C. Liu, I. Todd, J. Lertthanasarn, Damage-tolerant architected materials inspired by crystal microstructure, Nature 565 (7739) (2019) 305–311.

[14] L.R. Meza, A.J. Zelhofer, N. Clarke, A.J. Mateos, D.M. Kochmann, J.R. Greer, Resilient 3D hierarchical architected metamaterials, Proc. Natl. Acad. Sci. 112 (37) (2015) 11502–11507.

[15] J. Song, S. Reichert, I Kallai, D. Gazit, M. Wund, M.C. Boyce, C. Ortiz, Quantitative microstructural studies of the armor of the marine threespine stickleback (*Gasterosteus aculeatus*), J. Struct. Biol. 171 (3) (2010) 318–331.

[16] C.S. Tiwary, S. Kishore, S. Sarkar, D.R. Mahapatra, P.M. Ajayan, K. Chattopadhyay, Morphogenesis and mechanostabilization of complex natural and 3D printed shapes, Sci. Adv. 1 (4) (2015) e1400052.

[17] G.X. Gu, M. Takaffoli, M.J. Buehler, Hierarchically enhanced impact resistance of bioinspired composites, Adv. Mater. 29 (28) (2017) 1–7.

[18] G.X. Gu, F. Libonati, S.D. Wettermark, M.J. Buehler, Printing nature: Unraveling the role of nacre's mineral bridges, J. Mech. Behav. Biomed. Mater. 76 (March) (2017) 135–144.

[19] A. Zaheri, J.S. Fenner, B.P. Russell, D. Restrepo, M. Daly, D. Wang, C. Hayashi, M.A. Meyers, P.D. Zavattieri, H.D. Espinosa, Revealing the mechanics of helicoidal composites through additive manufacturing and beetle developmental stage analysis, Adv. Funct. Mater. 28 (33) (2018) 1–11.

[20] N. Suksangpanya, N.A. Yaraghi, B.R. Pipes, D. Kisailus, P. Zavattieri, Crack twisting and toughening strategies in Bouligand architectures, Int. J. Solids Struct. 150 (2018) 83–106.

[21] E. Feilden, C. Ferraro, Q. Zhang, E. García-Tuñón, E. D'Elia, F. Giuliani, L. Vandeperre, E. Saiz, 3D printing bioinspired ceramic composites, Sci. Rep. 7 (1) (2017) 13759.

[22] J.R. Raney, B.G. Compton, J. Mueller, T.J. Ober, K. Shea, J.A. Lewis, Rotational 3D printing of damage-tolerant composites with programmable mechanics, Proc. Natl. Acad. Sci. USA 115 (6) (2018) 1198–1203.

[23] S. Roundy, P.K. Wright, M. Montero, D. Odell, S.H. Ahn, Anisotropic material properties of fused deposition modeling ABS, Rapid Prototyp. J. 8 (4) (2003) 248–257.

[24] T.D. McLouth, J.V. Severino, P.M. Adams, D.N. Patel, R.J. Zaldivar, The impact of print orientation and raster pattern on fracture toughness in additively manufactured ABS, Addit. Manuf. 18 (2017) 103–109.

[25] Z. Wang, T.A. Palmer, A.M. Beese, Effect of processing parameters on microstructure and tensile properties of austenitic stainless steel 304L made by directed energy deposition additive manufacturing, Acta Mater. 110 (2016) 226–235.

[26] H. Choo, K.L. Sham, J. Bohling, A. Ngo, X. Xiao, Y. Ren, P.J. Depond, M.J. Matthews, E. Garlea, Effect of laser power on defect, texture, and microstructure of a laser powder bed fusion processed 316L stainless steel, Mater. Des. 164 (2019) 107534.

[27] M. Mirkhalaf, A. Khayer Dastjerdi, F. Barthelat, Overcoming the brittleness of glass through bio-inspiration and micro-architecture, Nature Commun. 5 (2014) 1–9.

[28] N. Suksangpanya, N.A. Yaraghi, D. Kisailus, P. Zavattieri, Twisting cracks in Bouligand structures, J. Mech. Behav. Biomed. Mater. 76 (March) (2017) 38–57.

[29] R.O. Ritchie, Mechanisms of fatigue-crack propagation in ductile and brittle solids, Int. J. Fract. 100 (1999) 55–83.

[30] L. Zorzetto, D. Ruffoni, Wood-inspired 3D-printed helical composites with tunable and enhanced mechanical performance, Adv. Funct. Mater. 29 (1) (2019) 1–9.

[31] ASTM-E399-17, Standard Test Method for Linear-Elastic Plane-Strain Fracture Toughness KIc of Metallic Materials, ASTM International, 2017.

[32] M.E. Launey, R.O. Ritchie, On the fracture toughness of advanced materials, Adv. Mater. 21 (20) (2009) 2103–2110.

[33] M.E. Launey, E. Munch, D.H. Alsem, H.B. Barth, E. Saiz, A.P. Tomsia, R.O. Ritchie, Designing highly toughened hybrid composites through nature-inspired hierarchical complexity, Acta Mater. 57 (10) (2009) 2919–2932.

[34] S. Shan, S.H. Kang, J.R. Raney, P. Wang, L. Fang, F. Candido, J.A. Lewis, K. Bertoldi, Multistable architected materials for trapping elastic strain energy, Adv. Mater. 27 (29) (2015) 4296–4301.